Early-type galaxies in low-density environments: NGC 6876 explored through its globular cluster system

Ana I. Ennis,[1,2]★ Lilia P. Bassino,[1,2] Juan P. Caso[1,2] and Bruno J. De Bórtoli[1,2]

[1]*Facultad de Ciencias Astronómicas y Geofísicas de la Universidad Nacional de La Plata, and Instituto de Astrofísica de La Plata (CCT La Plata – CONICET, UNLP), Paseo del Bosque S/N, B1900FWA La Plata, Argentina*
[2]*Consejo Nacional de Investigaciones Científicas y Técnicas, Rivadavia 1917, C1033AAJ Ciudad Autónoma de Buenos Aires, Argentina*

ABSTRACT

We present the results of a photometric study of the early-type galaxy NGC 6876 and the surrounding globular cluster (GC) system. The host galaxy is a massive elliptical, the brightest of this type in the Pavo Group. According to its intrinsic brightness ($M_v \sim -22.7$), it is expected to belong to a galaxy cluster instead of a poor group. Observational material consists of g', r', i' images obtained with the Gemini/GMOS camera. The selected GC candidates present a clear bimodal colour distribution at different galactocentric radii, with mean colours and dispersions for the metal-poor ('blue') and metal-rich ('red') typical of old GCs. The red subpopulation dominates close to the galaxy centre, in addition to the radial projected distribution showing that they are more concentrated towards the galaxy centre. The azimuthal projected distribution shows an overdensity in the red subpopulation in the direction of a trail observed in X-ray that could be evidence of interactions with its spiral neighbour NGC 6872. The turnover of the luminosity function gives an estimated distance modulus $(m - M) \approx 33.5$ and the total population amounts to 9400 GCs, i.e. a quite populous system. The halo mass obtained using the number ratio (i.e. the number of GCs with respect to the baryonic and dark mass) gives a total of $\sim 10^{13}$, meaning it is a very massive galaxy, given the environment.

Key words: galaxies: elliptical and lenticular, cD – galaxies: evolution – galaxies: star clusters: individual: NGC6876.

1 INTRODUCTION

Environment plays a major role in determining several features of galaxies, such as their Hubble type, colour, and star formation rate (Zhang et al. 2013), as well as in conditioning the evolutionary processes they undergo. Early-type galaxies (ETGs) are usually found in high-density environments, which is why most studies focus on galaxies inhabiting clusters. However, in low-density environments, accretion mechanisms can be less efficient than in clusters (Cho et al. 2012) and allow us to study growth and evolutionary processes in action (e.g. Bassino & Caso 2017).

Taking the environment into account proves to be key to understand galaxy evolution, since statistical studies (Tal et al. 2009) have shown that it is in massive ETGs inhabiting low-density environments that tidal features are most frequently found, meaning it is very common for them to be experiencing gravitational interactions. Hirschmann et al. (2013) finds through studying simulated field ETGs that a large fraction of them suffers late mergers, in which there is usually very little gas involved (Jiménez et al. 2011). These

interactions or 'dry mergers' could explain how the haloes of ETGs in low-density environments keep on growing while maintaining the average age and metallicity of their population (Thomas et al. 2010; Lacerna et al. 2016). The fact that processes of this sort are expected in galaxies in these environments has caused an increase in their study (Salinas et al. 2015; Caso, Bassino & Gómez 2017; Escudero et al. 2018).

The analysis of objects that are old enough to have belonged to their host galaxy since its formation, and that have survived ever since, is remarkably useful for untangling all the processes the galaxy has gone through since formation. In this sense, globular clusters (GCs) are perfect candidates, since their estimated ages are > 10 Gyr (Peng et al. 2006). They also offer the advantage of being compact and intrinsically bright enough that they can be detected as point-like sources in galaxies as far ≈200 Mpc (e.g. Harris et al. 2014).

One of the most studied characteristics of globular cluster systems (GCS) is their colour distribution, which is very often found to be bimodal in massive ETGs, indicating the presence of two subpopulations (e.g. Harris, Harris & Hudson 2015). Though this could be a result of either a difference in age or in metallicity, spectroscopic studies indicate that there is no age difference among

★ E-mail: ennis.ana@gmail.com

(old) GCs to explain such a gap (e.g. Woodley et al. 2010). Colour bimodality is then understood as a difference in metallicity, with blue GCs having significantly less metal content than red ones (e.g. Brodie et al. 2012). In addition to the separation in colour, these GC subpopulations show other differences, such as their kinematics and spatial distribution (e.g. Schuberth et al. 2010; Pota et al. 2015; Caso et al. 2017). The origin of these subpopulations has not been fully explained yet.

There are a few mechanisms that do reproduce the bimodality. The hierarchic merger (Beasley et al. 2002) is based on semi-analitical model of formation, combining elements from older models. Blue GCs are formed in the early universe ($z > 5$) until a process, most likely cosmic reionization (van den Bergh 2001), puts a stop to it. Afterwards, gas-rich major mergers trigger the formation of the red GCs. However, the more accepted models nowadays are the assembly scenario (Tonini 2013) and the merging scenario suggested by Li & Gnedin (2014). Both use results from the Millenium simulation, the first one being based on the fusion rates obtained from it, and proposing that the red subpopulation is formed in the host galaxy at around $z \approx 2$ whereas the blue one is accreted from satellite galaxies. The latter uses the halo merger trees obtained from the Millenium simulations and an empirical relation between the galaxy's mass and metallicity. In this model, the bimodality emerges because of red GCs forming in mergers of massive haloes, while blue GCs were formed in previous mergers, with less-massive haloes involved.

Recent works (Pfeffer et al. 2018; Kruijssen et al. 2019) combined the EAGLE model for galaxy formation simulations (Crain et al. 2015; Schaye et al. 2015) with the MOSAICS model for cluster formation and evolution (Kruijssen et al. 2011) in order to study the connection between the evolution of GCS and their host galaxy. In Kruijssen et al. (2018), the analysis of the Milky Way (MW) and its cluster population showed that at least 40 per cent of the clusters had formed *ex situ*, identifying their progenitors as massive galaxies accreted by the MW early on its history.

Recently, a third subpopulation has been found in several galaxies. All of them show signs of interactions that had been previously detected, and stellar population models fitted to this third subpopulation estimated an age for it that matches the time past since these merger or accretion events. This hints at the possibility that this would be the result of star formation events being triggered by interactions, which makes this third subpopulation a subject of interest since they would be GCs currently at a much earlier stage of formation than the ones usually observed (Caso, Bassino & Gómez 2015; Bassino & Caso 2017; Sesto et al. 2018).

NGC 6876 is a massive elliptical galaxy located in the Pavo galaxy group (Fig. 1). The different values for the distance modulus of NGC 6876 found in the NASA/IPAC Extragalactic Database (NED) present a wide dispersion. In this work, we adopt the mean of the two corrected values from Blakeslee et al. (2001), based on the Fundamental Plane and on the SBF method, respectively, obtaining a distance of ∼45 Mpc.

From the SIMBAD data base, its apparent blue magnitude is $B = 11.76$, and considering the median colours for elliptical galaxies given by Fukugita et al. (1996) and the absorption maps constructed by Schlafly & Finkbeiner (2011), it translates into an estimated absolute visual magnitude of $M_V \approx -22.7$.

Though ETGs as luminous as NGC 6876 are usually found in rich clusters, the Pavo galaxy group consists of barely thirteen galaxies, confirmed through radial velocities, with a velocity dispersion of 425 km s^{-1} (Machacek et al. 2009, and references therein). In addition, it appears to be a dynamically young group. Many
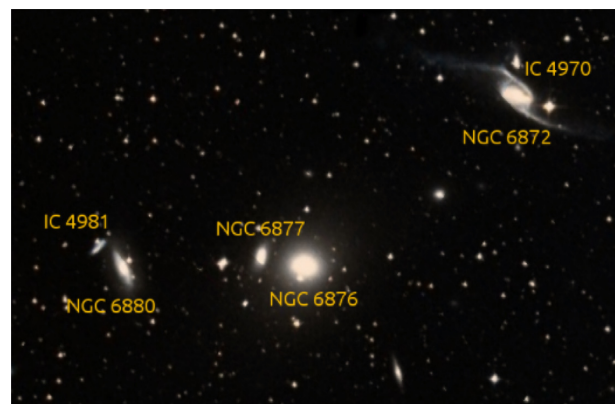

Figure 1. DSS image of the group centred on NGC 6876. North is up, and east is to the left.

members have less-massive companions, showing strong signs of interaction between them. NGC 6876 in particular has an elliptical companion, NGC 6877, at 1.4 arcmin to the east with a difference in radial velocity of $\Delta V_r \approx 300$ km s^{-1}, which could be in an early pre-merger phase Machacek et al. (2009).

However, the interesting suggestion that NGC 6876 might be interacting with other members is not related to these less-massive neighbours. Instead, *XMM–Newton* observations revealed a ≈ 90 kpc trail of X-ray emission hotter (≈1 KeV) than the Pavo intergalactic medium (IGM) that links NGC 6876 to its nearest massive neighbour, NGC 6872 (Machacek et al. 2005) which is located at a projected distance of 8.7 arcmin, ∼113 kpc given our assumed distance. The latter is a spiral galaxy which is currently interacting with its companion, IC 4970 (Mihos, Bothun & Richstone 1993; Machacek et al. 2008). Before the discovery of this trail, NGC 6876 was not believed to have any relation with the morphological distortions of NGC 6872, since there is a significant difference in their radial velocities (∼ 13 per cent, NED), and their projected distance is eight times larger than the projected distance between NGC 6872 and IC 4970. Besides being the first hint that these two massive galaxies might be interacting, this trail is important since there are very few trails associated to large spiral galaxies, and it is the first one observed in a low-density group (Machacek et al. 2005).

Machacek et al. (2005) concludes, from analysing the *XMM–Newton* observations of the X-ray trail, that it cannot be entirely made of tidally stripped gas from NGC 6876. Tidal interactions strong enough to have removed that amount of hot gas should have also altered the stellar distribution, and such distortions have not been found yet. Nonetheless, interactions cannot be ruled out, though it is also suggested that the trail is primarily associated with NGC 6872, since its surface brightness increases near the spiral galaxy. In a further analysis of the trail, Horellou & Koribalski (2007) find no signs of interaction with NGC 6872 in the HI distribution of NGC 6876. Though their simulations do not model the motions of NGC 6872 through the IGM or the gas environment, they suggest the trail might be a result of Bondi–Hoyle accretion around NGC 6872, where the IGM gas of the group suffers from gravitational focus because of the galaxy passing through the core of the group, resulting in its adiabatic heating (Bondi & Hoyle 1944).

For better resolution, Machacek et al. (2009) combines *Spitzer*'s mid-infrared and *Chandra* X-ray observations of NGC 6872 and NGC 6876 with archival optical as well as H I data. The emission excess at 8µm found in NGC 6876 is weak and mostly stellar. The

Table 1. Exposure times and central wavelengths for each filter.

Filter	λ_{eff} (nm)	Exposure time (s)
g'	475	8×800
r'	630	6×450
i'	780	9×500

non-stellar portion appears to come from leakage from emission produced by silicate dust grains ejected from the atmospheres of evolved AGB stars.

A more recent study of NGC 6872 (Eufrasio et al. 2014), however, goes back to the original assumption that these two galaxies might have interacted not that long ago. Using UV-to-IR archival data, this analysis of the spiral galaxy reveals NGC 6876 might have shaped its neighbour over a long period of time, contributing to the bar before the interactions between NGC 6872 and its minor companion had started. In this scenario, it is reasonable to expect to find some evidence of this interaction in NGC 6876 as well.

In this work, we perform a photometric study of the GCS of NGC 6876, based on Gemini observations. We analyse the colour distribution and, after separating the GC subpopulations, we present their individual spatial distributions, as well as the luminosity function of the entire system. In addition, we study the surface-brightness distribution of the galaxy. Preliminary results (Ennis, Bassino & Caso 2017a,b) have shown a clear bimodality in the colour distribution, with the two GC subpopulations following the same spatial distributions as typically found in the literature.

The structure of this paper is as follows. In Section 2, the observations and reduction process are described. In Section 3, we present the GC selection, and in Section 4, the analysis of the GCS. In Section 5, we study the host galaxy surface brightness distribution, while a discussion of our findings is presented in Section 6. Finally, in Section 7 we report our conclusions.

2 OBSERVATIONS AND DATA REDUCTION

The data set was taken over the course of several nights spread throughout 2013 August, September, and November, with the Gemini Multi-Object Spectrograph (GMOS) camera, mounted on the Gemini South telescope (programme GS-2013B-Q-37; PI: J.P. Caso).

A single field containing the galaxy was observed in g', r', and i' filters, as detailed in Table 1, with 2×2 binning that resulted in a scale of 0.146 arcsec pixel^{-1}.

Bias and flat-field corrections were applied using the corresponding images from the Gemini Observatory Archive (GOA[1]) and the Gemini routines included in the IRAF package, which were also employed for the usual processing of the data.

The images in the i' filter showed a significant fringing pattern. This effect, if left uncorrected, can affect negatively the photometric quality of the images (e.g. Howell 2012). For its treatment, images of a blank field were reduced in the same manner as the science field. The final fringe pattern was created with the task GIFRINGE using a combination of these dithered images, in order to dispose of any stars that may be present in them. The task GIRMFRINGE scales the image properly and subtracts it from the science image, thus eliminating the interference pattern.

[1] https://archive.gemini.edu/

For each filter, the images are slightly dithered so that their combination in addition to a bad pixel mask, gives a final product clean of cosmic rays and flaws generated by the detector. To perform a more exhaustive search for stellar-like objects, we eliminated most of the galaxy light applying a median filtering with the task FMEDIAN and subtracting it from the original image. We performed this task twice, using first a 200×200 pixels window and then a 40×40 pixels window, respectively.

In addition to our GMOS-S images, a smaller WFPC2 field that contains the galaxy was obtained from the *HST* Data Archive. The exposure times were 4200 s in both filters, *F*555*W* and *F*814*W*. In this case, a smooth model of the galaxy's light distribution was generated using the ELLIPSE task from the DAOPHOT package in IRAF and subtracted from the image. These observations were carried out in 1999 May (Proposal 6587, PI: D. Richstone). The data may be obtained from here.

3 GMOS PHOTOMETRY

3.1 Point-source selection

As GCs will appear as unresolved point-like objects at the distance of NGC 6876, we used SEXTRACTOR (Bertin & Arnouts 1996) to detect the GC candidates. This code offers a variety of filters to improve the detection of faint objects. In this work, we combined the selection obtained with a *Gaussian* filter and a *mexhat* filter. The latter is usually a better fit for objects in crowded areas, such as the regions closer to the galactic centre.

Besides producing a catalogue with estimated aperture photometry for each object, the software assigns a value between 0 and 1 to every object depending on how point-like they are. Those nearer to 0 are extended objects, likely to be background galaxies. The parameter that stores this value is called *CLASS STAR*. Our first requirement for point-like objects was *CLASS STAR* > 0.5.

Using tasks in the DAOPHOT package, we obtained approximated magnitudes of the selected objects through aperture photometry. Using these as initial values, more precise magnitudes were calculated using PSF photometry. Based on a selection of 100 bright stars distributed over the field, we obtained a second-order variable model for the PSF suitable for our images. ALLSTAR uses this PSF to measure the instrumental magnitude for every selected object.

As it performs a fit for every object, it also gives the results of the goodness fits, which were used to make a refined selection, choosing the values for χ^2 using the artificial stars added for completeness as described in Section 3.3.

Our final point-sources catalogue was made of $\sim$1670 objects in a magnitude range of $18.7 < i'_0 < 25.5$.

3.2 Photometric calibration

To calibrate our instrumental magnitudes, we worked with observations of the field 195940-595000 of standard stars from Smith et al. (2002), taken with the science data. Given its right ascension and altitude, this field is observable at the same time as NGC 6876, allowing the observations to be conducted under conditions as similar as possible to the science ones. Different exposure times were used to obtain images of the standards field, so that we did not lose neither too faint nor too bright objects. With the task PHOT we performed photometry over them, varying the aperture over a large range of sizes.

These results were used to build a growth curve, which tells us the size of aperture needed to capture all the light corresponding

Table 2. Coefficients of the standard transformations.

Filter	Zero point	Colour term
g'	3.31 ± 0.04	$0.13 \pm 0.06\,(g' - r')$
r'	3.38 ± 0.02	$0.07 \pm 0.03\,(g' - r')$
i'	2.98 ± 0.03	$0.01 \pm 0.04\,(r' - i')$

to the object. In this case, the curve becomes stable at around 30 pixels. This is the aperture used both for the final photometry of the standard stars and for the aperture correction applied to the magnitudes previously obtained for the point-source objects in our science field.

The Gemini telescope website[2] provides users with the necessary transformation equations as seen in equation (1), for which we determined the corresponding photometric zero-points for each band and the colour terms shown in Table 2 by interpolating the relation between our instrumental magnitudes and the standard ones, obtained from the catalogue in Smith et al. (2002).

$$m_{\text{std}} = m_{\text{zero}} - 2.5 \log_{10}\left(N(e-)/\text{exptime}\right)$$
$$- k_{\text{CP}}(\text{airmass} - 1.0) + CT(\text{colour}_1 - \text{colour}_2). \quad (1)$$

Finally, we applied a correction for galactic extinction, using the absorption coefficients provided by Schlafly & Finkbeiner (2011) with $E(B - V) = 0.04$, thus obtaining the final standard magnitudes for our GC candidates.

3.3 Completeness and background estimation

The estimation of the completeness of the GC candidate selection was made through the addition of artificial stars, which were then measured. In this case, 500 artificial stars were added using the task ADDSTAR within DAOPHOT, generated with random x, y positions scattered through the whole field, and a random magnitude within the usual limits for GC selection. This process was repeated 40 times, generating new stars every time for each filter. Afterwards, the reduction process used for the science images was applied to the 120 frames, filtering them and carrying out the detection of point sources and their photometry in exactly the same way as it was done before. No systematic trends were detected when analysing the differences between the input and output magnitudes in relation to other parameters, such as distance to the galaxy centre.

In order to ensure a completeness of 80 per cent, we take a faint brightness limit of $i' = 24.5$. In addition, we fit an analytic function to our completeness curves, as can be seen in Fig. 2, of the form:

$$f(m) = \beta \left(1 - \frac{\alpha(m - m_0)}{\sqrt{1 + \alpha^2(m - m_0)^2}}\right). \quad (2)$$

This function has β, α, and m_0 as free parameters, and it is similar to the one used by Harris et al. (2009). It allows us to have a more exact determination of the completeness level at different galactocentric distances for when more precise corrections are necessary.

The contamination level caused by background galaxies and nearby stars was estimated through the analysis of a comparison field, also observed with Gemini South in GN-2001B-SV-67 programme. However, the correction was deemed negligible, since only around 8–10 objects were found within the colour range corresponding to GCs.
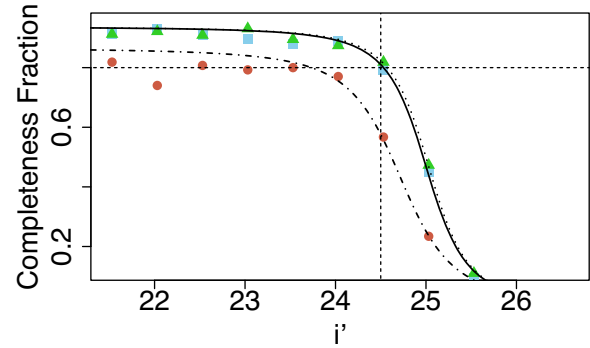
Figure 2. Completeness fraction for the inner region (dots), medium region (squares), and external region (triangles). Each region has its corresponding fit plotted in dot–dashed, solid and dotted, respectively. The dashed line shows the chosen limit.
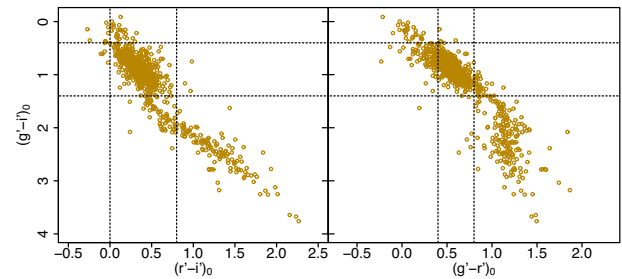

Figure 3. Colour–colour diagram for all the point-source objects detected with SEXTRACTOR. Dashed lines show the limits taken for the GC selection.

3.4 GC selection

Since GCs usually fall within clearly defined colour ranges, we set our selection using limits derived from those used in other works with the same photometric system (e.g. Faifer et al. 2011; Bassino & Caso 2017). As can be seen in the colour–colour diagrams in Fig. 3, the chosen limits are $0.0 < (r' - i') < 0.8$, $0.4 < (g' - i') < 1.4$ and $0.4 < (g' - r') < 0.8$. Regarding brightness limits, ultra-compact dwarfs (UCDs) are known to be present in the same colour range but they are brighter than GCs, so we apply an upper limit in magnitude derived from Mieske et al. (2006) to separate them from our GC candidates. For setting the faint magnitude limit, we will consider the 80 per cent completeness level at $i' = 24.5$.

Fig. 4 shows the colour–magnitude diagram of all the point sources, and the ∼760 GC candidates as golden diamonds. The errors depicted with horizontal lines on the right-hand side of the figure correspond to the average dispersion within each bin of 0.1 mag.

In the brighter end of the GC selection, it is noteworthy how there appears to be a significant lack of GCs on the blue side. This effect, usually referred to as the 'blue-tilt', has been recurrently interpreted as a mass–metallicity relation (MMR; Harris 2009; Usher et al. 2015; Harris et al. 2017a). Though many reasons for this shift in the MMR were proposed, recent analysis performed using the E-MOSAICS simulations have suggested the effect is caused by a lack of massive blue GCs. This absence is clear in our diagram, and it is proposed to be the consequence of a physical upper limit in cluster formation (Usher et al. 2018).

In the case of WFPC2 images, the point-source selection was performed over the filtered images of the field using the same method as described above. In order to select GC candidates, colour
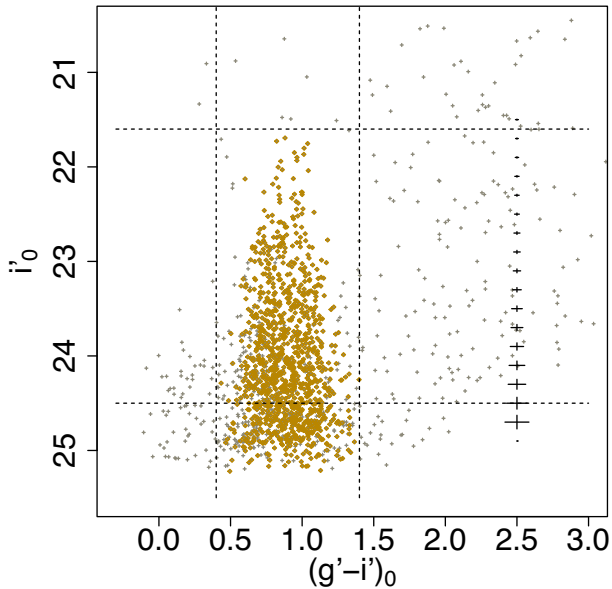
Figure 4. Colour–magnitude diagram for all the point-sources detected with SEXTRACTOR (grey crosses). The golden diamonds indicate the GC candidates, selected through the combination of limits in all colours as mentioned in the text. In magnitude, the faint limit corresponds to a completeness level of 80 per cent, whereas the bright limit separates possible UCD candidates. On the right, the crosses represent the errors in colour and magnitude.
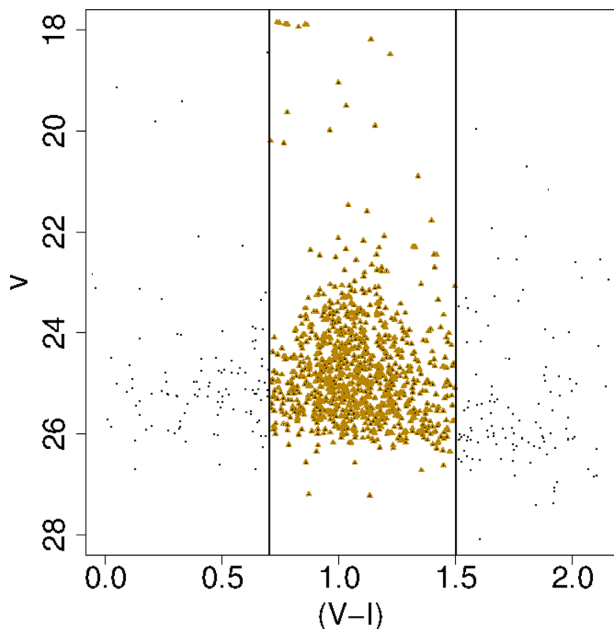

Figure 5. Colour–magnitude diagram for the point-source objects detected on the WFPC2 field (circles). The triangles indicate those that fulfil the colour criteria described in the text to be considered GC candidates.

limits were applied in the colour–magnitude diagram shown in Fig. 5. The (g', i') to (V, I) transformation was obtained from Bassino & Caso (2017), obtaining colour limits of $0.7 < (V - I) < 1.5$.

In addition, these images were also used to confirm the nature of the UCD candidates, previously selected only by colour and magnitude. In the case of those objects present in the field which
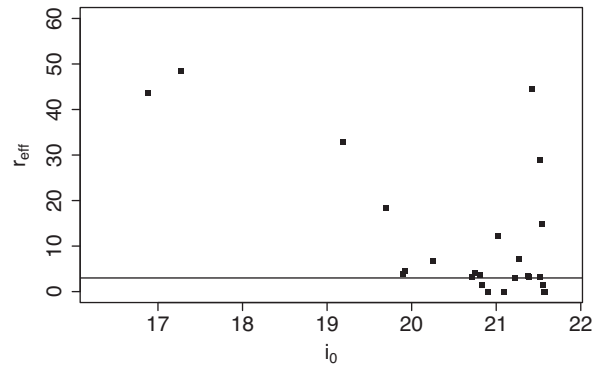

Figure 6. Distribution of the effective radius of all point-like sources with magnitudes brighter than the assumed limit for UCD candidates, against the GMOS i'_0 magnitude. The solid line indicates $r_{eff} = 3$ pc, the typical value for GCs (Jordán et al. 2007).

had $i'_0 < 21.6$, ISHAPE (Larsen 1999) was used in order to obtain estimations of their radii through the fitting of King profiles (King 1962, 1966), with a concentration parameter of $c = 30$ (Madrid et al. 2010). The results are shown in Fig. 6. There is an accumulation near $r_{eff} \sim 3$ pc, which is the typical effective radius of GCs (Jordán et al. 2007), and a sample of candidates that present radii larger than 10 pc, which is the order as the typical effective radius of small UCDs (Mieske et al. 2008). This indicates the presence of a UCD population with ~ 10 members in the inner region of the galaxy. It is important to note that, given the resolution of the WFPC2 being nearly the same size as the full width at half-maximum of stellar objects, these results are only accurate enough to be considered approximations.

4 GLOBULAR CLUSTER SYSTEM

4.1 Colour distribution

In Fig. 7, we present the colour distribution for all the GC candidates in the upper left-hand panel. The other three panels show the colour distribution for GC candidates at different galactocentric radii. For both the complete sample and the innermost region, the minimum distance is 15 arcsec so as to avoid the central zone, since it is saturated.

In order to determinate whether our distributions are multimodal or unimodal, we apply the algorithm Gaussian Mixture Modelling (GMM; Muratov & Gnedin 2010), which tests the sample for bimodality with two different statistics. The first one is the kurtosis of the distribution, which indicates how flat the distribution is. The more negative the kurtosis is, the flatter the distribution and the more likely it is to be multimodal, since a unimodal distribution is expected to have a peak. However, though a negative kurtosis is necessary for bimodality, it is not enough to confirm it.

The second statistic, D, which assumes bimodality and tells us how far apart the estimated means are, taking the dispersions into consideration as shown in equation (3). If it is greater than 2, the separation is wide enough that we can assume a bimodal distribution:

$$D = \frac{|\mu_1 - \mu_2|}{\left[(\sigma_1^2 - \sigma_2^2) / 2 \right]^{1/2}}. \tag{3}$$

The resulting statistics for the total GC population and three different radial ranges are shown in Table 3. In all cases, bimodality
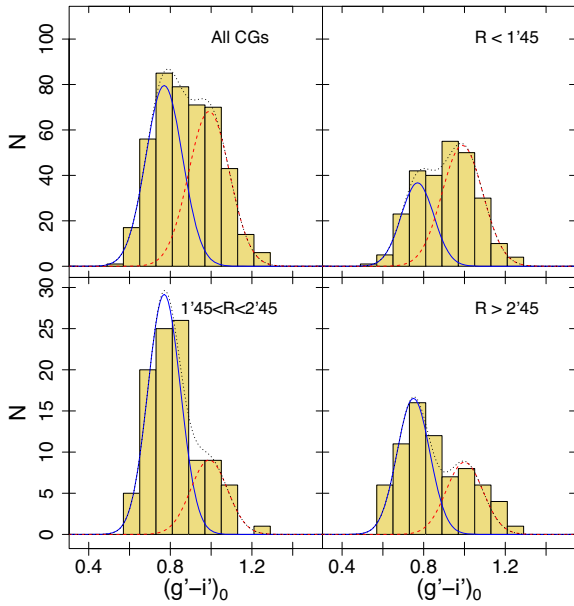
Figure 7. Colour distribution diagrams corresponding to the entire population in the top left-hand panel, and to rings at different galactocentric distances in the following panels, moving from the inner region (top right) to the outer region (bottom right). The blue solid and the red dashed lines represent the Gaussian fits corresponding to the metal-poor and to the metal-rich subpopulation, respectively. The dotted black line shows the sum of both functions.

seems to provide the best fit. It can be seen that the external region has the largest values in both tests, whereas the medium region has weaker results, which is caused by the large difference between the amount of GCs in each subpopulation. GMM also gives the estimated means and their corresponding dispersions for the fitted Gaussians, as shown in Table 3, and those parameters are the ones used in the Gaussians shown with solid lines in Fig. 7. The blue GC candidates are identified with a blue solid line and the red ones, with a dotted red line.

In all the histograms, the presence of the classic blue and red GCs is evident at the modal values of ∼0.8 and ∼1.0. While the red subpopulation dominates the sample in the inner region, the blue subpopulation surpasses it as we reach the more external regions, and it dominates the sample as a whole, as can be seen in other ETGs (e.g. Bassino et al. 2006; Usher et al. 2013).

The separation between both samples is considered to be at $(g' - i') = 0.9$, which is the colour obtained from GMM for which an object has an equal probability of belonging to either subpopulation.

4.2 Projected spatial and radial distribution

The projected spatial distribution for both blue and red GC candidates in our GMOS field is presented in Fig. 8. The centre of
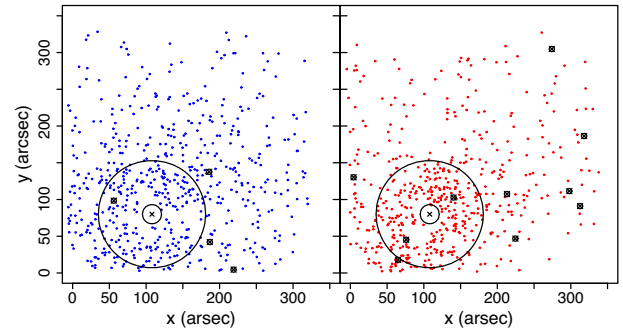

Figure 8. Projected spatial distributions for the blue (left-hand panel) and red (right-hand panel) GC candidates. The circles signal the region used for the azimuthal analysis in Section 4.3. The crossed-out circles depict the location of UCD candidates.
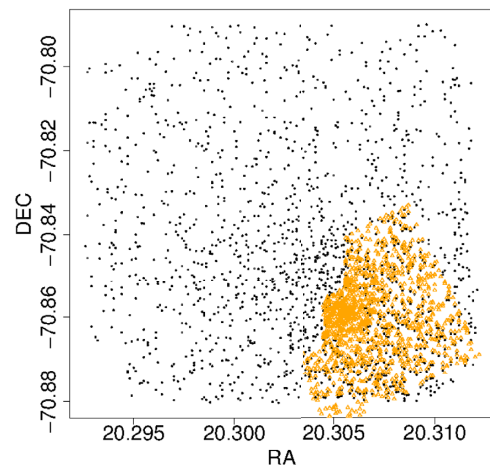

Figure 9. Spatial distribution of the GMOS sources (dots) and the WFPC2 sources (triangles), obtained with SEXTRACTOR.

NGC 6876 is indicated with a cross. It can be seen that even on the borders of the field that are furthest from the galaxy, the density of GCs is fairly high, indicating the system is larger than our field of view (FOV). The red GCs are more concentrated towards the galaxy, whereas the blue GCs extend throughout the entire field, dominating at larger radii. Since the central region was excluded from all analyses due to the incompleteness caused by saturation, this section was complemented with the WFPC2 photometry that allows us to examine the distributions in more detail. In Fig. 9, we show the spatial distribution of the sources obtained using these images, superimposed on our GMOS distribution in order to show the region covered by them.

In order to eliminate any possible contamination due to the neighbour galaxy, we considered the variations in density throughout the field and found they were negligible. Considering the intrinsic

Table 3. Means, standard deviations and statistics obtained with GMM.

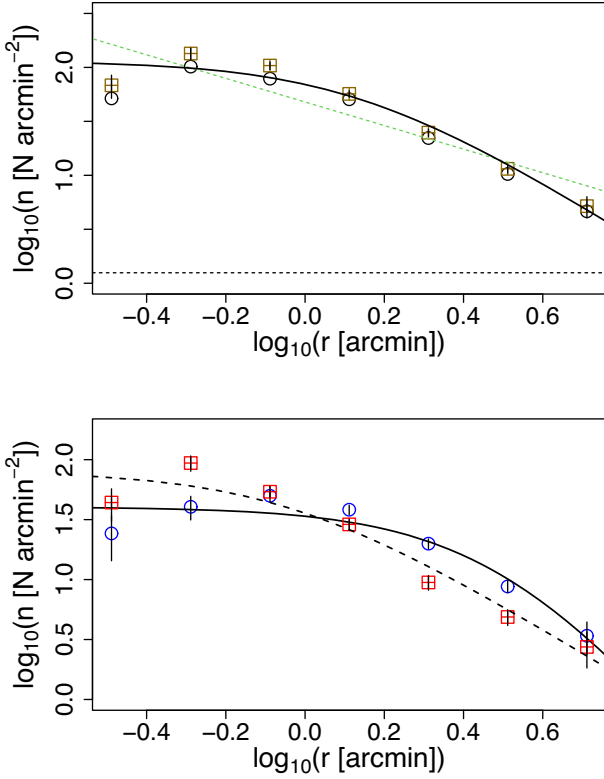| Region	Blue subpopulation		Red subpopulation		Kurtosis	D
	μ	σ	μ	σ		
All GCs	0.77 ± 0.02	0.09 ± 0.01	0.99 ± 0.02	0.10 ± 0.01	-0.67	2.39 ± 0.24
Inner	0.77 ± 0.04	0.08 ± 0.02	0.99 ± 0.03	0.09 ± 0.02	-0.51	2.35 ± 0.39
Medium	0.77 ± 0.04	0.08 ± 0.02	1.01 ± 0.08	0.09 ± 0.04	0.20	2.68 ± 0.95
External	0.75 ± 0.02	0.08 ± 0.01	1.03 ± 0.04	0.09 ± 0.02	-0.91	3.32 ± 0.59

Figure 10. Projected radial distribution for the entire GC population (top panel), both corrected for completeness (squares) and without applying the corrections (circles), and for the red (squares) and blue (circles) subpopulation (lower panel). For the entire population, the solid line shows a Hubble function fit, while the dashed line shows a power-law fit. In the case of the subpopulations, they both have Hubble function fits, the solid line depicts the corresponding to the blue GCs and the dashed line, the one for the red GCs. The dotted line depicts the background level.

magnitude of the galaxy, we can assume it does not present an amount of GCs significant enough that it might affect our results.

Fig. 10 shows the radial distribution for the entire population in the upper panel, and for both subpopulations in the lower panel. In both cases, the sample has been corrected by completeness using the function previously fitted to the completeness curve. Power laws were fitted to the three samples, with slopes of -1.11 ± 0.21 for the entire population, -1.25 ± 0.20 for the red sample and -0.78 ± 0.25 for the blue sample.

These fits reinforce our previous result, showing that the red GCs decay at larger radii much faster than the blue ones.

It can be seen that all three radial profiles flatten towards the inner regions of the galaxy. Since the completeness correction was performed considering the variations in distance, this flattening might be a sign of a real lack of GCs in the vicinities of the galactic centre, rather than it just being an observational effect. In order to take the change in the slope into consideration, a modified version of the Hubble–Reynolds law (equation 4, Binney & Tremaine 1987; Dirsch, Richtler & Bassino 2003) was fitted to the total population. In this function, $n(r)$ represents the surface number density, and r_0, a core radius. It converges to a power law of index $2b$ at large radii.

$$n(r) = a \left(1 + \left(\frac{r}{r_0} \right)^2 \right)^{-b}.$$ (4)

The coefficients of the best fits are indicated in Table 4.

Table 4. Coefficients of the Hubble–Reynolds law fitted to the GMOS radial distributions.

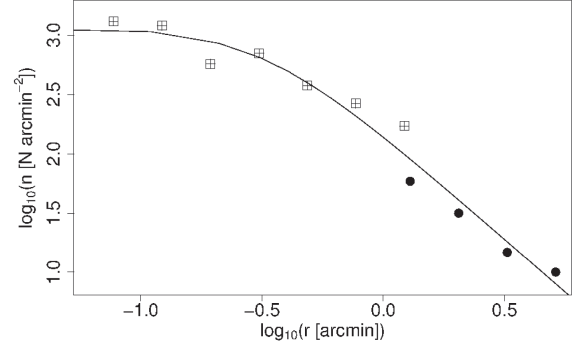| Population	a	r_0	b
All GCs	2.08 ± 0.09	1.29 ± 0.55	1.13 ± 0.32
Red GCs	2.22 ± 0.38	0.39 ± 0.29	0.86 ± 0.12
Blue GCs	1.70 ± 0.08	2.37 ± 1.11	1.57 ± 0.69

Figure 11. Radial distribution for the GMOS sources (dots) and the WFPC2 sources (squares). The solid line indicates the Hubble–Reynolds law fit.

Since the WFPC2 sources cover the inner region of the galaxy, we combined their radial distribution with the one obtained for our GMOS sources in Fig. 11, thus obtaining a distribution less affected by saturation, and we fitted a Hubble–Reynolds law as described in equation (4). The resulting parameters of this fit were $a = 3.1 \pm 0.1$, $b = 0.9 \pm 0.1$, and $r_0 = 0.3 \pm 0.1$.

The difference between this result and the one obtained merely for the GMOS sources indicates that a significant portion of the flattening in the inner region shown in Fig. 10 is a consequence of the difference in the noise levels, which is larger in the GMOS observations near the centre of the galaxy. However, this new radial profile still presents signs of flattening, though at a slower pace, indicating the disruption of GCs near the centre of the galaxy is significant.

Though our FOV does not reach background levels, we can extrapolate the Hubble–Reynolds fits to obtain an estimation of the full extension of the GCS. For this, we assume the background level to be at $N/\mathrm{arcmin}^2 \sim 1.25$, as obtained for similar works (Caso et al. 2015; Bassino & Caso 2017). The estimated extension is $r_{GCS} \sim 125\,\mathrm{kpc}$. Through integrating the Hubble–Reynolds law until that point, we can also obtain an approximate number for the total population of the GCS within this extension and brighter than $i'_0 = 24.5$ that gives us ~ 1960 GCs.

4.3 Projected azimuthal distribution

In order to achieve azimuthal completeness, we decided to only consider GCs with galactocentric radii between 13, 6, and 75 arcsec, as shown in Fig. 8. The projected azimuthal distribution is shown in Fig. 12.

We studied this distribution using the expression from McLaughlin, Harris & Hanes (1994):

$$\sigma(R, \theta) = kR^{-\alpha}[\cos^2(\theta - \mathrm{PA}) + (1 - \epsilon)^{-2}\sin^2(\theta - \mathrm{PA})]^{-\alpha/2},$$ (5)

where σ is the number of GC candidates, and a power-law radial distribution is assumed, with α being the value obtained in
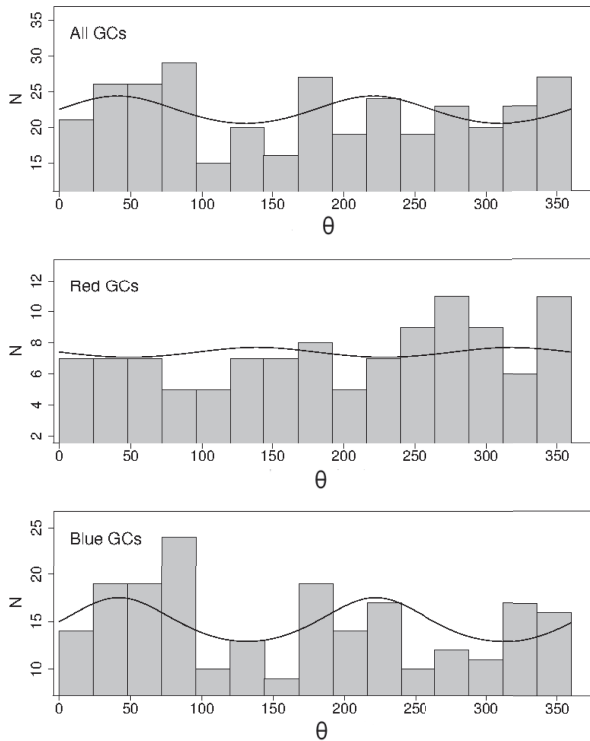
Figure 12. Projected azimuthal distribution for the entire GC population (top panel) and for the red (middle panel) and blue (circles) GC subpopulations (lower panel). The solid lines correspond to the fits described in the text.

Table 5. Values of position angle and ellipticity obtained for the complete sample and for the two subpopulations (those for the red subpopulation are not significant).

Parameter	Total	Red GCs	Blue GCs
PA	$40.7° \pm 23°$	$48.9° \pm 7.8°$	$42° \pm 8.6°$
ϵ	0.14 ± 0.10	0.01 ± 0.15	0.24 ± 0.11

Section 4.2. The position angle (PA) is measured counterclockwise from the north and fitted alongside the ellipticity. The number of GC candidates σ is calculated for circular regions of 24 degrees, as shown in Fig. 12.

In Table 5, we present the results of the fit applied to the complete GC sample and to each of the subpopulations. It can be seen that the red GC subpopulation shows no signs of elongation, while the blue subpopulation has a much more significant ellipticity. The behaviour of the complete sample seems to be led by the blue subpopulation.

An interesting though subtle feature in the red GC subpopulation is the slight overdensity between $250°$ and $360°$ (Fig 12). This happens to be in the same direction as the X-ray trail detected by Machacek et al. (2005), and the coincidence is even more clear in comparison with fig. 7 in Machacek et al. (2009). This effect only being noticeable in the red subpopulation could be a consequence of the size of region taken into account for the azimuthal distribution. Since it is very close to the galactic centre, the ring contains an important fraction of red GCs but a less relevant fraction of blue ones, the latter being therefore a noisier sample. There is no evidence of this implied disturbance in the stellar component of the galaxy, but this is not entirely unexpected. As said by Alamo-Martínez &
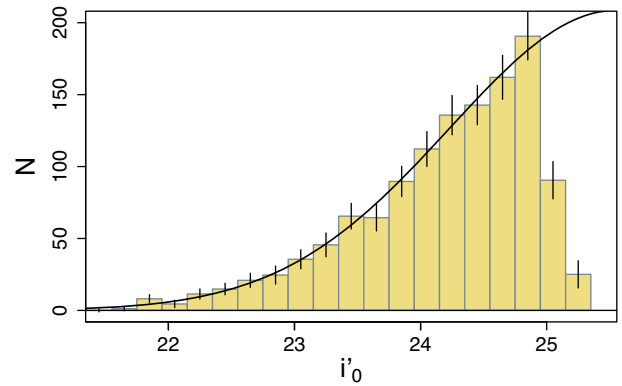

Figure 13. Luminosity function of the GC candidates. The vertical bars symbolize the error corresponding to each bin, and the solid line represents the Gaussian fit.

Blakeslee (2017), numerical simulations show that dark matter haloes are more affected than stars by gravitational interactions between galaxies, and among the stellar population, GCs are usually the first to be affected by the stripping because the GC system is spatially more extended than field stars (Smith et al. 2013; Mistani et al. 2016).

4.4 Luminosity function and GC population

Fig. 13 shows the luminosity function of the system. One of the most striking characteristics of GCSs is the apparent universality of the luminosity function, which has a nearly identical shape in most galaxies despite the variety of formation histories and tidal effects (Harris et al. 2014). Though it does depend slightly on galaxy mass (e.g. Villegas et al. 2010), the peak of the Gaussian function usually selected to perform the fits (*turnover*) is universal enough that it has been used as a standard candle for measuring extragalactic distances. It has been estimated that in ETGs, the turnover of the GC luminosity function in the V band is $M_V \sim -7.4$ (e.g. Richtler 2003; Jordán et al. 2007).

Though it can be seen from Fig. 13 that our i'_0 images are not deep enough to reach the turnover, we can estimate it through fitting a Gaussian to the distribution. The estimated turnover is found at $i'_0 = 25.6 \pm 0.4$, which translates to a distance modulus of $(m - M) = 33.5 \pm 0.4$ using equation (2) in Faifer et al. (2011), which allows us to obtain V_0 assuming a mean value for the GCs with $i'_0 > 25.5$ of $(g' - i')_0 \approx 0.9$.

Though the dispersion in the numerous distance measurements that can be found in NED for this galaxy is large, this value is a good approximation to the one measured by Blakeslee et al. (2001) using surface brightness fluctuations (SBFs).

Integrating the luminosity function allows us to estimate what percentage of the total GC population is covered up until the limit established by the completeness level. In this case, the integrations revealed our ≈ 2000 GC candidates are barely ≈ 21 per cent of the complete population, which gives us a total of $\approx 9500 \pm 2500$ GCs.

Another parameter usually analysed when studying GCSs is their *specific frequency*, defined simply as $S_N = N_{GC} 10^{0.4(M_V + 15)}$ (Harris & van den Bergh 1981). Thought to be almost constant among ETGs at first, it is now accepted that it varies with luminosity, and is linked to the efficiency in GC formation and retention. The 'average' value for elliptical galaxies was classically thought to be $S_N \approx 3.5$. Currently, the range has extended up to 10 and even higher, showing a significant dependence with the brightness of the
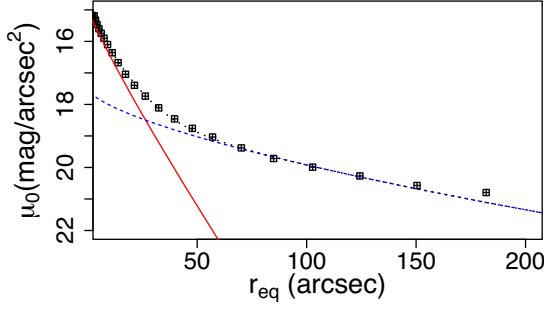
Figure 14. Surface brightness profile of NGC 6876 in i'_0. The solid line and the dashed line represent the inner and outer components, respectively, while the dotted line represents the sum of both.

Table 6. Parameters of the two Sérsic models fitted to the galaxy profile in the i' filter.

Parameter	μ_0	r_0	n
Inner	15	7.32	1.1
Outer	17.5	30	1.5

galaxy (Harris, Harris & Alessi 2013). For NGC 6876, we obtain a value of $S_N \approx 7.74$, which falls within the range though it is high for the estimated absolute visual magnitude we considered for it.

5 SURFACE BRIGHTNESS PROFILE OF NGC 6876

Using the ELLIPSE task from the DAOPHOT package in IRAF, we studied the surface brightness profile of the host galaxy NGC 6876 in the i' filter. Other bright galaxies present in the field were masked with the same task. Within a galactocentric radius of 1 arcmin, the isophotes were fitted leaving all parameters free, which allows us to analyse the behaviour of the ellipticity and the position angle, as depicted in Fig. 15. For isophotes at larger radii, those parameters were set fixed to the last values obtained, since the fact that they have regions that fall off the observed field, makes it impossible to get a proper fit. The surface brightness, however, can still be modelled accurately enough as shown in Fig. 14, which shows the surface brightness versus equivalent radius ($r_{eq} = \sqrt{ab} = a\sqrt{1-\epsilon}$, where a is the isophote semimajor axis and ϵ is the ellipticity). Two Sérsic models were fitted (Sersic 1968):

$$\mu(r) = \mu_0 + 1.0857 \left(\frac{r_{eq}}{r_0} \right)^{1/n},$$

where μ is expressed in mag arcsec^{-2}, μ_0 is the central surface brightness, r_0 is a scale parameter, and n is the Sérsic shape index. The resulting parameters for the inner and outer components are presented in Table 6. They point to the existence of an inner disc and an outer spheroid.

Through comparison with the surface brightness profile obtained from the Carnegie–Irvine Galaxy Survey (Ho et al. 2011), it becomes evident that the background level has not been reached in our field of view. In the Atlas profile, the background level is ~ 24 mag arcsec^{-2} in the I filter.

The parameters of the isophotes, i.e. position angle, ellipticity, and A_4 Fourier coefficient, were measured with ELLIPSE and are presented in Fig. 15. The upper panel shows the position angle PA, as we move further from the galaxy centre. The sudden change observed at around $r_{eq} \sim 40$ arcsec matches the end of the drop in
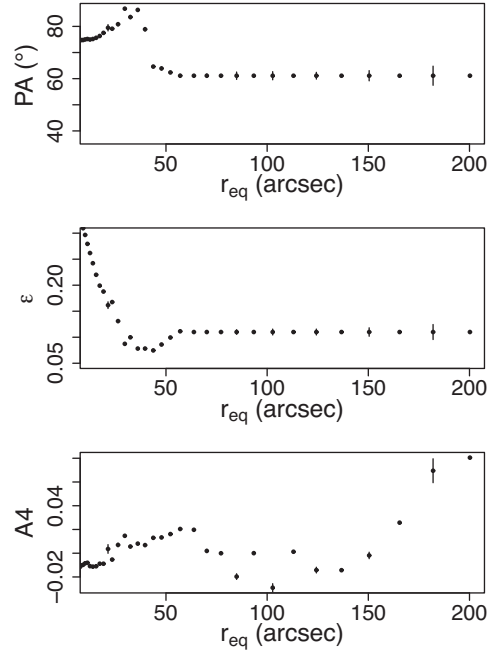

Figure 15. Upper panel: Position angle of the elliptical isophotes versus effective radius. Middle panel: Ellipticity of the elliptical isophotes versus effective radius. Lower panel: Parameter A_4 versus effective radius.

ellipticity ϵ at around the same radius, shown in the middle panel of Fig. 15. The radius corresponding to such changes in PA and ϵ approximately agree with the galactocentric radius at which the inner component becomes fainter than the outer one, and the total surface brightness is dominated by the outer spheroid. Since the isophotes turn more circular as we increase the radius, the errors in the estimation of the PA turn into very large values. In the case of the A_4 parameter, we see the inner regions have a negative value, which would indicate the central isophotes are boxy. Then it switches to positive after $r_{eq} \sim 30$ arcsec. Though it turns negative again at larger radii, the errors become too large to gather any conclusions.

6 DISCUSSION

Our photometric analysis of the GCS of NGC 6876 reveals a hint of interaction with NGC 6872 in the red subpopulation, though the rest of the results do not show further evidence.

The GMM test gives a solid bimodal fit for the colour distribution, and once separated the two GC subpopulations show normal behaviour, corresponding to what is usually found in the literature. However, the total GC population as calculated through the integration of the luminosity function is quite high, meaning NGC 6876 has a very populated system. Its extension is big, with a value calculated through the extrapolation of the radial distribution of about ~ 125 kpc.

In order to obtain a better approximation of the full extent, we use the relation between the GCS spatial extent versus galaxy stellar mass given by Kartha et al. (2014), deriving the host stellar mass by means of the mass-to-light ratio given by Zepf & Ashman (1993). Then, we obtain $\log (M/M_\odot) = 12$, which results in an extension of ≈ 88 Kpc for the GCS, which is a severe underestimation according to our results. However, this is not the only rich GCS that shows a larger extension than the one obtained from the Kartha et al. (2014)
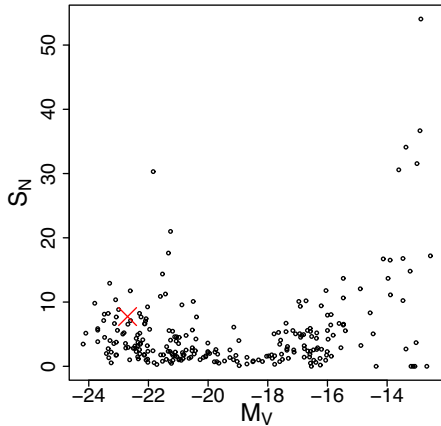
Figure 16. Specific frequency of GCSs in ETGs versus galactic absolute *V* magnitude, with NGC 6876 represented by a red cross.
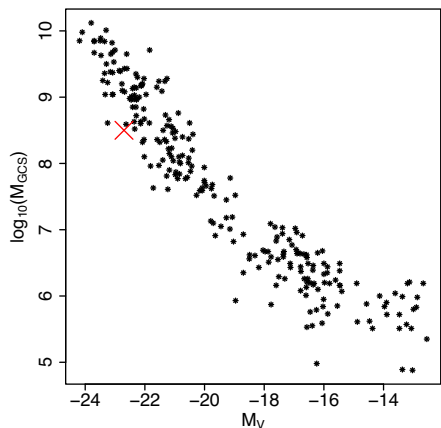

Figure 17. Mass of GCSs in ETGs versus galactic absolute *V* magnitude, with NGC 6876 marked with a red cross.

correlation (e.g. Bassino et al. 2006; Blom, Spitler & Forbes 2012; Caso et al. 2017).

We can also estimate the halo mass (i.e. baryonic plus dark mass), using the method described by Harris, Blakeslee & Harris (2017b). From the luminosity function, we obtained a total population of $N_{GC} \sim 9400$ GCs. Adopting a GC mean mass of $< M_{GC} > \sim 3.5 \times 10^4$ M$_\odot$, it results in a total mass for the galaxy's GCS of $M_{GCS} \sim 3.25 \times 10^8$ M$_\odot$. Dividing this result by the number ratio, a constant introduced by Blakeslee, Tonry & Metzger (1997) and defined as $n_N = N_{GC}/Mh$, recalibrated by Harris et al. (2017a) to a value of $n_N = 2.9 \times 10^{-5} \pm 0.28$, we end up with a halo mass of $M_h \sim 1.12 \times 10^{13}$ M$_\odot$. This mass is in agreement with other ETGs with highly populated GCSs (Pedersen, Yoshii & Sommer-Larsen 1997; Nakazawa et al. 2000; Caso et al. 2017).

Using the existing catalogue of globular systems in galaxies presented by Harris et al. (2013) and selecting those in ETGs only, we compared the obtained S_N and M_{GCS} with those for similar galaxies, most of them inhabiting clusters. It can be easily seen that in both cases (see Figs 16 and 17), the values fall among the expected ones for ETGs of this luminosity. Most ETGs in the bright end are located in dense environments, where they are expected to have undergone a rich history of mergers (Jiménez et al. 2011; Schawinski et al. 2014). This explains their highly

populated GCS, dominated by the metal-poor subpopulation, in the context of its build-up in two phases (Forbes et al. 2011; Caso et al. 2017). The fact that NGC 6876 presents both a highly populated GCS and a large stellar mass could indicate its history has also involved major mergers, despite its environment being of such low density.

Having the total population and the stellar mass allows us to estimate another parameter, T_N, as defined by Zepf & Ashman (1993). This parameter is another option when looking to find a relation between GCs and the morphology and mass of their host galaxy. In our case, we obtain $T_N \sim 9.4$, which falls among the expected values for ETGs with stellar masses similar to NGC 6876 (Peng et al. 2008).

Using the *XMM–Newton* observations analysed in Machacek et al. (2005), and the expression given by Grego et al. (2001), we can obtain an estimation of the stellar mass through an alternate method and compare it with the one derived from the mass-to-light ratio. In this case, we use $\mu = 0.6$ as the molecular weight, a temperature of $kT_e = 0.76\,kE_v$, and we calculate the mass up to the radial limit derived from the radial projected distribution of GCs, $r = 125$ kpc. The surface brightness profile for the X-ray emission was fitted using the combination of two β-models, with a core radius of $r_c = 5$ kpc and a value of $\beta = 0.65$ for the galactic component of NGC 6876, and $r_c = 50$ kpc and $\beta = 0.3$ for the surrounding intracluster medium. Considering the combination of both profiles, a result for the stellar mass of $M \sim 10^{12}$ M$_\odot$ is achieved, which is in agreement with the one previously calculated.

One very debated scaling relation between GCSs and their host galaxies is the matter of relative size, which has been studied in comparison with both the stellar and the halo mass. Since we have estimations for both as well as for the GCS extension, it is of interest to see where our data falls in the proposed existing relations. Recently, Forbes (2017) suggested an approximately linear relation between GCS size and halo mass to the one-third power, in contraposition to the simultaneous proposal by Hudson & Robison (2018), which has a much higher slope (0.80). In the case of stellar mass, again Hudson & Robison (2018) determines a bigger slope than Forbes (2017). For the halo mass, NGC 6876 falls far from both the relation proposed by Hudson & Robison (2018) that gives an estimated result of $\log r_{GCS} \sim 1.3$, and from the Forbes (2017) relation for which the size is ($\log r_{GCS} \sim 1.2$). However, the errors involved in the estimation of the halo mass are quite large, so this result should only be considered as an approximation.

In the case of the stellar mass, NGC 6876 seems to fall closer to Forbes (2017), $\log r_{GCS} \sim 1.9$, but it still results in a much smaller GCS when compared with our results, suggesting galaxies with highly populated GCSs show more massive haloes and do not follow the linear relations proposed so far.

Machacek et al. (2005) fitted the X-ray emission up to 100 kpc from the centre of the galaxy using a beta profile with two components, leading to an estimated value of $r_{500} \sim 370$ kpc. This indicates a dark matter halo that is at least that large, but looking at the profile, we can assume it extends much further. Another tracer of the dark matter halo is the distribution of blue GCs (Bassino et al. 2006; Usher et al. 2013) since they are thought to map out the total mass of the galaxy. When we compare the b parameter in our radial distribution to the one corresponding to bright ETGs in the centre of clusters (Fig. 18), the value is similar to those with approximately the same magnitude as NGC 6876. This reinforces the suggestion that, despite being in a low-density environment, the dark matter halo is similarly large to the haloes found in galaxies in much more dense habitats.
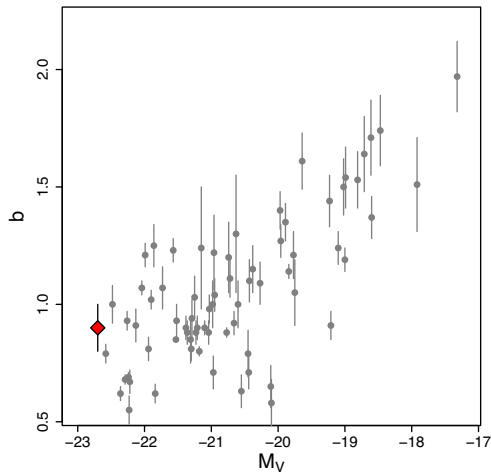
Figure 18. Parameter b as obtained from fitting a Hubble law profile to the radial distribution of ETGs, shown as black dots. NGC 6876 is highlighted in a larger red diamond.

Despite having only a suggestion of a connection between NGC 6876 and the trail connecting it to its spiral neighbour NGC 6872, in the projected spatial distribution of the GCs, we can still draw some conclusions about the evolutionary history of the galaxy. The radial extent of the GCS indicates the presence of a massive halo with a significantly large extension (Hudson, Harris & Harris 2014). As discussed in the Introduction section, in low-density environments elliptical galaxies are thought to have increased their mass after $z \sim 2$ through the so-called dry mergers. These involve satellite galaxies that, by the time of this interaction, are already red and quiescent thus providing a small amount cold gas and dust (if any) to the more massive galaxy and prompting little to no star formation (Huang et al. 2016). Based on its colour, $(B - I) \sim 2.24$ according to the Carnegie–Irvine Survey (Ho et al. 2011), and its magnitude, NGC 6876 is red enough that we can assume 'dry' mergers as the main causes of growth.

From the webtool CMD 3.0,[3] assuming Bressan et al. (2012) isochrones and Chabrier IMF, solar metallicity, typical of bright ellipticals, and the reddening corrections from Schlafly & Finkbeiner (2011), we estimate the age of the population for different colours, obtained from the Carnegie–Irvine Survey in the case of *B*, *V*, *R*, and *I*, and from 2MASS in the case of *J* and *H* (Huchra et al. 2012). The estimated age is between 7 and 10 Gyr. This indicates that the galaxy is dominated by an old stellar population, which goes in agreement with the increase in mass since $z \sim 2$ being prompted by 'dry' mergers, with no recent stellar formation.

A summary of important characteristics of NGC 6876 including our obtained parameters can be found in Table 7.

7 CONCLUSIONS

We performed a photometric study of the ETG NGC 6876 and its GCS, on the basis of Gemini-GMOS images in the bands g', r', and i'. The properties of the GCS were studied in detail, including the colour as well as radial and azimuthal projected distributions, luminosity function and determination of the total GC population and specific frequency. In addition, we made use of relations between characteristics of the GCS and of its host galaxy to estimate the stellar and halo (dark plus baryonic) mass, comparing

Table 7. Properties of NGC 6876.

Parameter	Value
M_V (mag)	− 22.7
Distance (Mpc)	45
$\log (M_{stellar}/M_\odot)$	12
$\log (M_{halo}/M_\odot)$	13
$E (B - V)$	0.04
r_{GCS} (kpc)	125
T_N	9.4
S_N	7.74

the different proposed relations that are being currently discussed. Our conclusions are summarized in the following:

(i) The colour distribution of the system is bimodal, revealing the usual subpopulations, with mean values similar to the ones typically found in the literature. Further analysis of the behaviour of the colour distribution in different galactocentric rings shows the red subpopulation decreases as we move towards the outer borders of the field.

(ii) In projection, the blue subpopulation is much more extended than the red one, as can be seen in both the spatial distribution and the radial one. This last one also allows us, through the fitting and integration of a Hubble profile to the distribution of the entire profile, to obtain an estimation for the population of the system within our completeness limit. From the azimuthal distribution, we can see the blue subpopulation is much more elongated, whereas the red one presents a slight overdensity that cannot be overlooked. Interestingly, such overdensity is located in the same direction of the observed X-ray trail between NGC 6876 and NGC 6872, and could be indeed a sign of their interaction.

(iii) The observed sample does not reach the turnover in the GC luminosity function. None the less, the extrapolation of the fitted Gaussian function provides us with a value for it that is consistent with the distance estimated by Blakeslee et al. (2001). The integration of this fit also lets us obtain an estimation of the total population of the system, ∼9500 GC candidates.

(iv) The current relations proposed for GCS size and halo mass all seem to underestimate the measurements obtained extrapolating our radial distribution, which is ∼125 kpc.

ACKNOWLEDGEMENTS

[3] http://stev.oapd.inaf.it/cmd

REFERENCES

Alamo-Martínez K. A., Blakeslee J. P., 2017, ApJ, 849, 6

Bassino L. P., Caso J. P., 2017, MNRAS, 466, 4259

Bassino L. P., Faifer F. R., Forte J. C., Dirsch B., Richtler T., Geisler D., Schuberth Y., 2006, A&A, 451, 789

Beasley M. A., Baugh C. M., Forbes D. A., Sharples R. M., Frenk C. S., 2002, MNRAS, 333, 383

Bertin E., Arnouts S., 1996, A&AS, 117, 393

Binney J., Tremaine S., 1987, Galactic Dynamics, Princeton University Press, Princeton, N.J., USA

Blakeslee J. P., Tonry J. L., Metzger M. R., 1997, AJ, 114, 482

Blakeslee J. P., Lucey J. R., Barris B. J., Hudson M. J., Tonry J. L., 2001, MNRAS, 327, 1004

Blom C., Spitler L. R., Forbes D. A., 2012, MNRAS, 420, 37

Bondi H., Hoyle F., 1944, MNRAS, 104, 273

Bressan A., Marigo P., Girardi L., Salasnich B., Dal Cero C., Rubele S., Nanni A., 2012, MNRAS, 427, 127

Brodie J. P., Usher C., Conroy C., Strader J., Arnold J. A., Forbes D. A., Romanowsky A. J., 2012, ApJ, 759, L33

Caso J. P., Bassino L. P., Gómez M., 2015, MNRAS, 453, 4421

Caso J. P., Bassino L. P., Gómez M., 2017, MNRAS, 470, 3227

Cho J., Sharples R. M., Blakeslee J. P., Zepf S. E., Kundu A., Kim H.-S., Yoon S.-J., 2012, MNRAS, 422, 3591

Crain R. A. et al., 2015, MNRAS, 450, 1937

Dirsch B., Richtler T., Bassino L. P., 2003, A&A, 408, 929

Ennis A., Bassino L., Caso J., 2017a, Galaxies, 5, 30

Ennis A. I., Bassino L. P., Caso J. P., 2017b, Boletin de la Asociacion Argentina de Astronomia La Plata Argentina, 59, 106

Escudero C. G., Faifer F. R., Smith Castelli A. V., Forte J. C., Sesto L. A., González N. M., Scalia M. C., 2018, MNRAS, 474, 4302

Eufrasio R. T., Dwek E., Arendt R. G., de Mello D. F., Gadotti D. A., Urrutia-Viscarra F., Mendes de Oliveira C., Benford D. J., 2014, ApJ, 795, 89

Faifer F. R., Forte J. C., Norris M. A., Bridges T., Forbes D. A., Zepf S. E., Beasley M. A., 2011, MNRAS, 416, 155

Forbes D. A., 2017, MNRAS, 472, L104

Forbes D. A., Spitler L. R., Strader J., Romanowsky A. J., Brodie J. P., Foster C., 2011, MNRAS, 413, 2943

Fukugita M., Ichikawa T., Gunn J. E., Doi M., Shimasaku K., Schneider D. P., 1996, AJ, 111, 1748

Grego L., Carlstrom J. E., Reese E. D., Holder G. P., Holzapfel W. L., Joy M. K., Mohr J. J., Patel S., 2001, ApJ, 552, 2

Harris W. E. et al., 2014, ApJ, 797, 128

Harris W. E., 2009, ApJ, 699, 254

Harris W. E., van den Bergh S., 1981, AJ, 86, 1627

Harris W. E., Kavelaars J. J., Hanes D. A., Pritchet C. J., Baum W. A., 2009, AJ, 137, 3314

Harris W. E., Harris G. L. H., Alessi M., 2013, ApJ, 772, 82

Harris W. E., Harris G. L. H., Hudson M. J., 2015, ApJ, 806, 36

Harris W. E., Ciccone S. M., Eadie G. M., Gnedin O. Y., Geisler D., Rothberg B., Bailin J., 2017a, ApJ, 835, 101,

Harris W. E., Blakeslee J. P., Harris G. L. H., 2017b, ApJ, 836, 67

Hirschmann M., De Lucia G., Iovino A., Cucciati O., 2013, MNRAS, 433, 1479

Horellou C., Koribalski B., 2007, A&A, 464, 155

Howell S. B., 2012, PASP, 124, 263

Ho L. C., Li Z.-Y., Barth A. J., Seigar M. S., Peng C. Y., 2011a, ApJS, 197, 21

Huang S., Ho L. C., Peng C. Y., Li Z.-Y., Barth A. J., 2016, ApJ, 821, 114

Huchra J. P. et al., 2012, ApJS, 199, 26

Hudson M. J., Robison B., 2018, MNRAS, 477, 3869

Hudson M. J., Harris G. L., Harris W. E., 2014, ApJ, 787, L5

Jiménez N., Cora S. A., Bassino L. P., Tecce T. E., Smith Castelli A. V., 2011, MNRAS, 417, 785

Jordán A. et al., 2007, ApJS, 171, 101

Kartha S. S., Forbes D. A., Spitler L. R., Romanowsky A. J., Arnold J. A., Brodie J. P., 2014, MNRAS, 437, 273

King I., 1962, AJ, 67, 471

King I. R., 1966, AJ, 71, 64

Kruijssen J. M. D., Pelupessy F. I., Lamers H. J. G. L. M., Portegies Zwart S. F., Icke V., 2011, MNRAS, 414, 1339

Kruijssen J. M. D., Pfeffer J. L., Reina-Campos M., Crain R. A., Bastian N., 2019, MNRAS, 486, 3180

Lacerna I., Hernández-Toledo H. M., Avila-Reese V., Abonza-Sane J., del Olmo A., 2016, A&A, 588, A79

Larsen S. S., 1999, A&AS, 139, 393

Li H., Gnedin O. Y., 2014, ApJ, 796, 10

Machacek M. E., Ashby M. L. N., Jones C., Forman W. R., Bastian N., 2009, ApJ, 691, 1921

Machacek M. E., Nulsen P., Stirbat L., Jones C., Forman W. R., 2005, ApJ, 630, 280

Machacek M. E., Kraft R. P., Ashby M. L. N., Evans D. A., Jones C., Forman W. R., 2008, ApJ, 674, 142

Madrid J. P. et al., 2010, ApJ, 722, 1707

McLaughlin D. E., Harris W. E., Hanes D. A., 1994, ApJ, 422, 486

Mieske S. et al., 2008, A&A, 487, 921

Mieske S., Hilker M., Infante L., Jordán A., 2006, AJ, 131, 2442

Mihos J. C., Bothun G. D., Richstone D. O., 1993, ApJ, 418, 82

Mistani P. A. et al., 2016, MNRAS, 455, 2323

Muratov A. L., Gnedin O. Y., 2010, ApJ, 718, 1266

Nakazawa K., Makishima K., Fukazawa Y., Tamura T., 2000, PASJ, 52, 623

Pedersen K., Yoshii Y., Sommer-Larsen J., 1997, ApJ, 485, L17

Peng E. W. et al., 2006, ApJ, 639, 95

Peng E. W. et al., 2008, ApJ, 681, 197

Pfeffer J., Kruijssen J. M. D., Crain R. A., Bastian N., 2018, MNRAS, 475, 4309

Pota V. et al., 2015, MNRAS, 450, 1962

Richtler T., 2003, in Alloin D., Gieren W., eds, Lecture Notes in Physics, Vol. 635, Stellar Candles for the Extragalactic Distance Scale. Springer Verlag, Berlin, p. 281

Salinas R., Alabi A., Richtler T., Lane R. R., 2015, A&A, 577, A59

Schawinski K. et al., 2014, MNRAS, 440, 889

Schaye J. et al., 2015, MNRAS, 446, 521

Schlafly E. F., Finkbeiner D. P., 2011, ApJ, 737, 103

Schuberth Y., Richtler T., Hilker M., Dirsch B., Bassino L. P., Romanowsky A. J., Infante L., 2010, A&A, 513, A52

Sersic J. L., 1968, Atlas de Galaxias Australes. Observatorio Astronomico de Cordoba, Cordoba, Argentina

Sesto L. A., Faifer F. R., Smith Castelli A. V., Forte J. C., Escudero C. G., 2018, MNRAS, 479, 478

Smith R., Sánchez-Janssen R., Fellhauer M., Puzia T. H., Aguerri J. A. L., Farias J. P., 2013, MNRAS, 429, 1066

Smith J. A., Tucker D. L., Kent S., Richmond M. W., Fukugita M., Ichikawa T., Ichikawa, 2002, AJ, 123, 2121

Tal T., van Dokkum P. G., Nelan J., Bezanson R., 2009, AJ, 138, 1417

Thomas D., Maraston C., Schawinski K., Sarzi M., Silk J., 2010, MNRAS, 404, 1775

Tonini C., 2013, ApJ, 762, 39

Usher C. et al., 2015, MNRAS, 446, 369

Usher C., Forbes D. A., Spitler L. R., Brodie J. P., Romanowsky A. J., Strader J., Woodley K. A., 2013, MNRAS, 436, 1172

Usher C., Pfeffer J., Bastian N., Kruijssen J. M. D., Crain R. A., Reina-Campos M., 2018, MNRAS, 480, 3279

van den Bergh S., 2001, ApJ, 559, L113

Villegas D. et al., 2010, ApJ, 717, 603

Woodley K. A., Harris W. E., Puzia T. H., Gómez M., Harris G. L. H., Geisler D., 2010, ApJ, 708, 1335

Zepf S. E., Ashman K. M., 1993, MNRAS, 264, 611

Zhang B. et al., 2013, ApJ, 777, 122

This paper has been typeset from a TEX/LATEX file prepared by the author.